Crystal-based absolute photon energy calibration methods for hard x-ray free-electron lasers

Christian Grech* and Marc Walter Guetg
Deutsches Elektronen-Synchrotron DESY, Notkestraße 85, 22607 Hamburg, Germany

Gianluca Aldo Geloni, Ulrike Boesenberg, Naresh Kujala, Mikako Makita, and Svitozar Serkez
European XFEL, Holzkoppel 4, 22869 Schenefeld, Germany

(Received 24 November 2023; accepted 12 April 2024; published 16 May 2024)

Bragg diffraction from crystals is widely used to select a very narrow spectral range of x-ray pulses. The diffracted signal can be used to calibrate the photon energy, a fact that can be exploited very effectively at x-ray free-electron lasers (XFELs). This work describes three crystal-based methods used to this goal at a major x-ray FEL facility, the European XFEL. These methods, which have a wide applicability, have been developed in relation to the hard x-ray self-seeding setup installed at the SASE2 undulator. They are fast and straightforward to implement since they are based on techniques for extracting and identifying crystal reflections from standard diagnostic raw data while still delivering few electronvolts resolution.

DOI: 10.1103/PhysRevAccelBeams.27.050701

I. INTRODUCTION

The ability to readily obtain absolute energy calibration by means of a crystal setup with reasonable accuracy and in a short time frame is crucial for an x-ray free-electron laser (FEL) facility. For example, in nuclear resonant scattering experiments [1], the identification of narrow resonance peaks often requires accurate photon energy information to locate resonances without the need for extensive energy scanning [2], which is particularly beneficial when searching for weak resonance peaks. Additionally, accurate photon energy data are essential for determining the lattice spacing of samples, aiding in the structural analysis of crystalline, noncrystalline, and nanomaterials [3].

Methods for the absolute determination of the photon energy have been implemented for many years, based on Bragg's law, which relates incident angle, the x-ray wavelength, and the spacing of the diffracting lattice planes [4]. For example, absolute determination of the energy has been carried out *in situ* using multiple-beam diffraction setups [5,6] or measuring the angle between two reflecting positions of the crystal in a bond diffractometer [7]. A bond diffractometer typically consists of a rotating stage that holds the crystal sample and allows precise angular positioning. The calculated precise angles at which the x rays are diffracted by the crystal are used for calibrating x-ray photon energies [8]. In this work, we propose and demonstrate three photon energy calibration techniques, utilizing the crystal setup shown in Fig. 1 and, depending on the method, either a spectrometer or an imaging station consisting of a camera looking through a scintillator. The setup and diagnostics shown in Fig. 1 are already available at the European XFEL for hard x-ray self-seeding (HXRSS) operation [9–14]. The HXRSS system at the European XFEL functions by inserting a single-crystal monochromator between two undulator sections. When the crystal is aligned to a Bragg reflection, it filters x rays to a narrow band of approximately 1 eV from the self-amplified spontaneous emission (SASE) pulse broader spectrum, which averages several tens of eV in width. The forward diffracted signal is delayed and appears after the main x-ray peak that traveled through the crystal without undergoing diffraction. This delayed part of the diffracted intensity becomes the initial seeding signal, which is superimposed to the electron beam in the second undulator section. Using Bragg's law, various reflections can be exploited by changing the rotation of the crystal, allowing continuous tuning of the HXRSS setup in photon energy. The methods proposed in this work allow for the identification of the crystal reflections by collecting and analyzing spectra or reflected intensities within a small range of

*christian.grech@desy.de

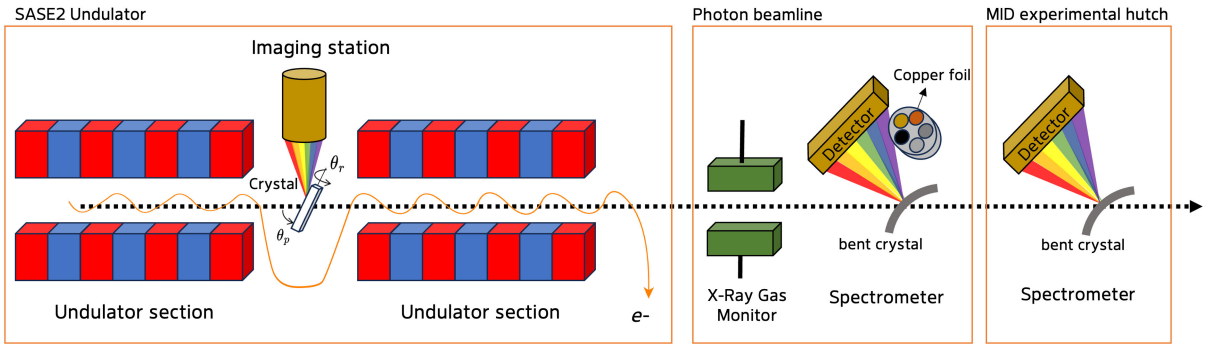

FIG. 1. Crystal setup and diagnostic devices used at the European XFEL SASE2 undulator and crystal rotation conventions. The schematic also shows the diagnostic devices in the photon beamline and experimental hutch, which were used in the copper K-edge scan in Sec. III.

the crystal pitch angle. Knowing the crystal reflection and its orientation, the absolute photon energy can be determined through Bragg's law, with an accuracy limited by the bandwidth of the radiation pulse. These methods cannot compete with the more precise measurements mentioned before but they are fast to implement, they often suffice to carry out experiments, and they are complemented with more precise techniques from the user's side, whenever needed.

The first method, called spectrometer reflection classifier, makes explicit use of data from the HXRSS system commissioning and operation at the European XFEL, see Fig. 1. Lutman *et al.* [15] first used the HXRSS data to characterize the self-seeding diamond crystal orientation at the Linac Coherent Light Source (LCLS) and determine the absolute photon energy. Here, we expand the method by applying a machine learning (ML) model that can be used once a crystal is characterized, for reflection identification and subsequent determination of energy differences. This enables operation outside of areas where reflections intersect, expanding the scope of applicability.

The other two approaches can be used at any FEL facility even without active HXRSS amplification. The second approach, called the spectral notch method, is similar to the first but is based on a notch produced by the crystal monochromator. As the delayed part of the diffracted intensity becomes the seeding pulse for the second undulator section, the original SASE spectrum shows a narrow "notch." In this approach, the spectrometer reflection classifier method is also used, but it does not need a self-seeded signal. In fact, this kind of notch was detected at the SASE2 HXRSS system, and also at a setup after the SASE1 undulator, and used for photon energy estimation [16].

The third calibration method is based on scintillator imager scans, where the reflection intensity at different pitch angles (detected at the imaging station in Fig. 1) is correlated with the photon energy. It makes the presence of a spectrometer redundant, at the price of a decreased resolution, due to a larger SASE bandwidth.

We demonstrate the three methods experimentally at the European XFEL. They are widely used at the European XFEL to calibrate the photon energy of the HXRSS signal but, more in general, they are suited as diagnostics methods at modern x-ray sources.

Our work is organized as follows: In Sec. II, we discuss general principles and delve deeper into each method, including the specific data processing techniques related to each of them. In Sec. III, we discuss a verification of the spectrometer reflection classifier by scanning around the K-edge of a copper foil. Finally, Sec. IV includes outlook and conclusions.

II. METHODS

A. General principle

Bragg reflection takes place when the distance traveled by waves scattered off adjacent layers of a crystal lattice plane is an integral multiple of the radiation wavelength [4]. This gives rise to the constructive interference of the reflected waves leading to the Bragg condition:

$$n\lambda = 2d \sin\theta, \tag{1}$$

where θ is the angle between the incident ray and the diffracting atomic plane of the crystal, λ is the wavelength of the radiation, d is the interatomic spacing between the crystal planes, and n is the order of reflection. In the following, we will assume $n = 1$. The lattice spacing of a particular cubic system can be obtained through the following relation:

$$d = \frac{a}{\sqrt{h^2 + k^2 + l^2}}, \tag{2}$$

where a is the lattice spacing of the cubic crystal, and $[h, k, l]$ are the Miller indices of the Bragg plane.

The crystal orientation with respect to the incident beam direction shown in Fig. 1 plays a fundamental role in all methods discussed in this paper. The incident angle θ is a function of the crystal orientation when Eq. (1) is satisfied, $\theta = \theta_{\text{Bragg}}$, and this corresponds to fixed values of the pitch, roll and yaw angle of a certain reflection. In the setup used in this work, the pitch and the roll angle of the crystal are controlled. The pitch rotational stage, with a pitch angle θ_p ranges between $30° \leq \theta_p \leq 120°$, and the roll rotational stage, with a roll angle θ_r ranges over 2°. The yaw angle θ_y is kept constant and unchanged throughout operations. The pitch rotation axis is orthogonal to the beam incident direction and parallel to the floor, while the roll rotation axis is parallel to the beam incident direction when $\theta_p = 0°$.

Let us call with k^i and n_0^j with $i, j = 1..3$, respectively, the components of the unit vector in the incident direction of the radiation and of the unit vector orthogonal to the Bragg plane in a suitable Cartesian reference system attached to the crystal. If we define the components n_0^j through the Miller indices by $\vec{n}_0 = (h, k, l)/\sqrt{h^2 + k^2 + l^2}$, in order to obtain the components k^i in the reference system of the crystal, we need to rotate the unit vector $\vec{k}_0$ that defines the direction of the incident radiation in the laboratory system (along the z axis) to obtain $k^i = \mathcal{R}^i_j k^j_0$ with $\mathcal{R}(\theta_p, \theta_r, \theta_y)$ a matrix modeling subsequent rotations around pitch, roll and yaw axes of the crystal (we used the Einstein summation convention). Then, the following relation holds:

$$E_{ph} = \frac{h_p c}{2d|\mathcal{R}_{ij} k^j_0 n^i_0|}, \tag{3}$$

where h_p is the Planck constant, c the speed of light in vacuum, and we express the Planck constant in $eV \cdot s$ while performing actual calculations. Equation (3) is, in essence, Bragg's law.

For a similar HXRSS system at the LCLS, Lutman *et al.* proposed a physics-based model involving multiple free parameters. The values of the free parameters are calculated for the installed system by fitting measured intersections at various pitch and roll angles [15]. This work considers four free parameters that are applied to the three rotational parameters to match the theoretical model with the actual expected crystal behavior. The resulting surrogate model based on Eq. (3) is given by

$$\tilde{E}_{ph} = E_{ph}(\hat{\theta}_p, \hat{\theta}_r, \hat{\theta}_y), \tag{4}$$

where $\tilde{E}_{ph}$ is the modeled photon energy, and the variables are the three effective rotational parameters $(\hat{\theta}_p, \hat{\theta}_y, \hat{\theta}_r)$. The effective pitch angle $(\hat{\theta}_p)$ is defined with the introduction of the pitch angle offset $(\delta\theta_p)$, a constant associated with a fixed deviation from the actual pitch angle

$$\hat{\theta}_p = \theta_p + \delta\theta_p. \tag{5}$$

The effective roll angle is represented by two factors: a scaling factor for the pitch angle (θ_{r1}) and an offset $(\delta\theta_{r2})$ so that

$$\hat{\theta}_r = \theta_r + \theta_{r_1}\theta_p + \delta\theta_{r_2}. \tag{6}$$

Similarly, the yaw angle is offset by a constant $(\delta\theta_y)$ according to

$$\hat{\theta}_y = \theta_y + \delta\theta_y. \tag{7}$$

The model parameters are found by optimizing the modeled output with historical measured scans. Figure 2(a) shows an intersection of reflections at 9 keV, measured using a single-shot spectrometer, while the fitted model is shown in Fig. 2(b).

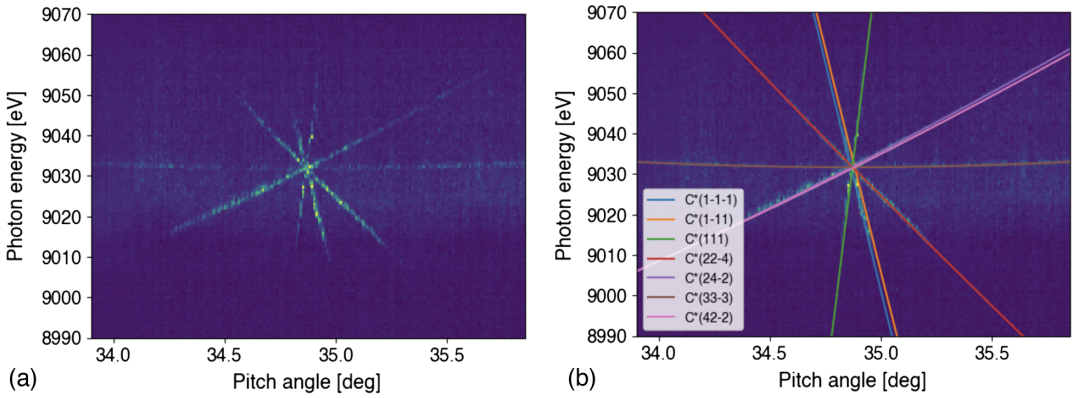

FIG. 2. (a) An intersection of reflections at 9 keV measured using a spectrometer, as a function of the pitch angle θ_p for fixed values of the roll and yaw angles and (b) the fitted model.

B. Experimental setup

The crystal used in this work is a 100-cut HTHP IIa type (high temperature, high pressure) C* (diamond) plate. Diamond is typically favored due to its low thermal expansion, high thermal conductivity, and minimal x-ray absorption, making it capable of withstanding intense x-ray pulses. The crystal used in this work has a thickness of 100 μm with variation lower than 5 μm and a misorientation angle lower than 0.5° [17]. A diagnostic device around the monochromator consists of an imaging station capable of detecting the x-ray pulse reflected by the crystal. The imaging station making use of a Basler avA2300–25 gm 12-bit charge-coupled device (CCD) camera is installed with a top view of the monochromator crystal in the European XFEL's SASE2 undulator beamline as sketched in Fig. 1. A YAG:Ce (Cr-doped Yttrium Aluminium Garnet) scintillator with an active field of view of 89×67 mm^2 (horizontal $\times$ vertical) [18] completes the imager. Different crystal reflections can be detected as bright spots in different horizontal and vertical locations, which vary depending on the reflection and photon energy, providing a good candidate for a photon energy calibration method. The energy spectra of the transmitted radiation are measured using the HIgh REsolution hard X-ray single-shot (HIREX) spectrometer following the SASE2 undulator of the European XFEL [19], see again Fig. 1. It uses bent crystals as a dispersive element and an MHz-repetition-rate stripline detector (or as an alternative, a low repetition-rate 2D camera).

Over a 2-year period of HXRSS operation at the European XFEL, spectral measurements involving the monochromator crystal were carried out, covering a photon energy range of 6–18 keV. The pySpectrometer photon diagnostic software developed for the European XFEL [20] allows correlations to be performed between the measured photon energy and a parameter of interest. As the monochromator crystal is rotated along the pitch axis, the photon energy measured from the single-shot spectrometer can be correlated with the angle of rotation and exported for further processing.

C. Spectrometer reflection classifier method

The algorithm that evaluates the calibration of the crystal setup and its use for photon energy determination is shown in Fig. 3. It relies on data from a single-shot spectrometer and the model in Eq. (4), set up using the best-fit values for the experimental setup. Reflection lines are extracted from spectral data using image processing techniques, while a classifier is trained with data from the characterized model. First, the reflection is determined and, second, knowing the pitch angle, the absolute operational photon energy can be determined.

1. Feature extraction

Several techniques can be implemented to extract reflection lines from crystal pitch angle or energy spectrometer scans. Computer vision and ML techniques can be exploited for feature extraction and classification. Such methods have been widely used in diagnostic applications for particle accelerators [21]. Several works have also used ML techniques in x-ray crystal setups, such as to predict symmetry [22] and to identify Bragg peaks [23,24]. Measured spectrometer scans provide correlations that highlight all reflections present in a limited energy range, as shown in the examples in Fig. 2. The image quality varies from one example to another, mostly affected by the presence of noise and different intensities of the seeding signal compared to the SASE background. A computer vision technique that is able to detect all the reflections and ignore any measurement artifacts is required.

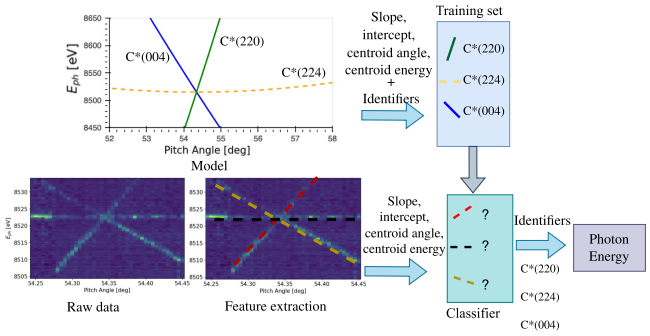

FIG. 3. Schematic technique of the spectrometer reflection classifier method proposed in this work.

In order to segment the information in the foreground from the background, thresholding is applied using the method proposed by Yen *et al.* [25]. This creates a binary image as shown in Fig. 4(b), extracted from the raw data in Fig. 4(a). In addition, morphological closing is performed to fill small holes while preserving the shape and size of the objects in the image. The closing operation dilates an image and then erodes the dilated image, using the same kernel for both operations.

For the identification of lines within the binary images, the classical Hough transform method [26] is employed. For each pixel in the foreground, a number of lines

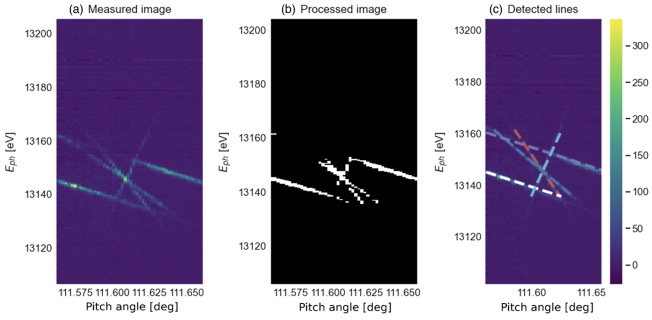

FIG. 4. (a) Raw data from single-shot spectrometer, (b) processed version (binarization, dilation, erosion), and (c) detected lines (Hough transform).

are plotted going through it, all at varying angles (ϕ). The distance between an origin point and each pixel is calculated (r), and when multiple points have similar (r, ϕ) values, these are considered to pertain to the same line [27]. In this way, a number of lines can be detected from the image as shown in Fig. 4(c). As a result, several line properties, namely the line slope, intercept, and centroid coordinates can be determined.

The identification of straight lines from the captured images by thresholding the image is not a perfect method for noting all visible lines, as some faint lines can be mistaken for noise or background. In addition, the accuracy is lower in cases where the contrast between foreground and background is low. By default, lines with a slope of zero or infinity are ignored to avoid identifying measurement artifacts as reflections. From over 200 images from both monochromator crystals containing 446 lines (visible and faint lines), the Yen thresholding method was able to extract 303 of these lines, corresponding to an accuracy of 68%. What makes this method desirable for our applications is the very low number of false positives (line detection where no reflection is present), which amounts to 3 lines in over 200 images.

2. Crystal reflection classification

After feature extraction, a machine learning classifier is used to match detected image lines with tangent lines derived from the surrogate model. The classifier considers the features of a given reflection line and predicts the corresponding Miller indices h, k, l for a reflection C*(hkl). It is trained with the properties of the tangent lines of the measurement model as features (slope, intercept, centroid pitch angle, and centroid energy) and the reflection identifier as the target or predictor. The algorithm calculates the proximity between the model or measured features and picks the closest class, in this case, a reflection identifier. A classifier is trained with a limited portion of data from the model relevant to the pitch angle and energy of interest.

Three classifiers are compared in this study: the k-nearest neighbor, random forest, and decision tree algorithms. Based on the collection of available reflections for the second monochromator, reflections that have been measured more than 5 times have been considered (93 examples in total). The performance criteria used for the comparison are the precision score, recall score, and balanced accuracy score. The precision score for multiclass classification can be defined as the sum of true positives (TP) across all classes, divided by the sum of true positives and false positives (FP) across all classes,

$$\text{Precision} = \sum_{c=1}^{C} \text{TP}_c / \sum_{c=1}^{C} (\text{TP}_c + \text{FP}_c). \tag{8}$$

The recall score sums the true positives across all classes and divides by the sum of true positives and false negatives across all classes,

TABLE I. ML classifier performance comparison.

Classifier	k-Nearest neighbor	Random forest	Decision tree
Precision score	0.78	0.63	0.78
Recall score	0.70	0.52	0.65
Balance accuracy	0.90	0.81	0.84

$$\text{Recall} = \sum_{c=1}^{C} \text{TP}_c / \sum_{c=1}^{C} (\text{TP}_c + \text{FN}_c). \tag{9}$$

The balanced accuracy score in multiclass classification cases is introduced to deal with imbalanced datasets. This is important to include in this case as some reflections are represented more than others. The balanced accuracy score is the average recall score obtained on each class.

The k-nearest neighbors algorithm was found to be the best fit for this scenario. The k-nearest neighbor algorithm creates "neighborhoods" for objects with similar features. The category of an unclassified point is found by comparing the point features against those of the previously classified k neighbors, which exist as a subset of a larger space of previously classified points. Table I shows the performance comparison between the three classifiers. Across all performance metrics, the k-nearest neighbor algorithm was found to perform better than the other two algorithms. The confusion matrix in Fig. 5 shows the predicted reflection identifiers versus the actual identifiers for the k-nearest neighbor classifier. One can note that in two scenarios, reflections are classified incorrectly, the first in the case of C*(1-11) being classified as C*(1-1-1) and in the second case C*(3-11) being classified as C*(1-3-1). While we expect a vertical (photon energy) error from our measurement, this means that the classifier has no criteria to differentiate between the two. In all other cases, the reflections are correctly classified. In order to avoid an incorrect calculation, in the software console, if detected, these reflection lines are left out of the energy calibration calculation.

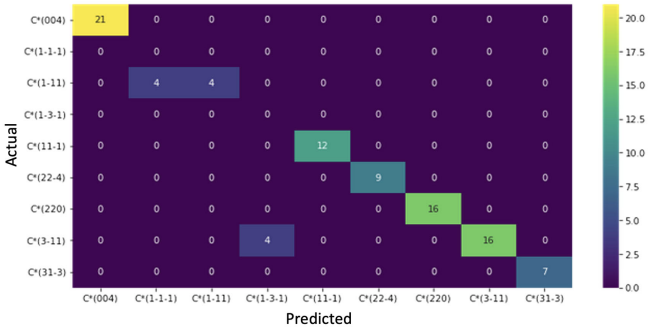

FIG. 5. A confusion matrix showing the total predicted reflections versus the actual reflection classification.

D. Spectral notch method

The second method proposed in this work also makes use of the single-shot spectrometer as a diagnostic device, however, without relying on the self-seeded signal. In fact, in this case, the second undulator section is detuned. As discussed before, when the Bragg condition in Eq. (3) holds for frequencies within the SASE spectrum, the signal transmitted by the HXRSS crystal roughly consists of the original SASE spectrum (adjusted for absorption) with a "notch," which works as a fiducial marker. The notch detected by the spectrometer is typically about 0.5 to 1 eV wide, as can be seen in the example in Fig. 6.

Figure 7 shows a spectral notch detected by filtering the SASE spectrum through one of the HXRSS crystals, using the C*(1-1-3) reflection. Figure 7(a) shows spectral data correlated with the crystal pitch angle as it is scanned in a range of 0.2°. The notch moves in energy as a function of the pitch angle over a 20 eV range. Figure 7(b) shows the reflection data from the model plotted on top of the measured data, where a calibration of +1 eV has been applied compared to the data in Fig. 7(a). Feature extraction requires an extra step for this method, as the images have to be inverted to make sure that the notch pixels are in the foreground for the Hough Transform to detect a line. However, as noted above, compared to the spectrometer reflection classifier method, the spectral notch method has the advantage that it does not need a HXRSS setup to work, but only a crystal and a spectrometer, which can be installed at any position down an undulator system.

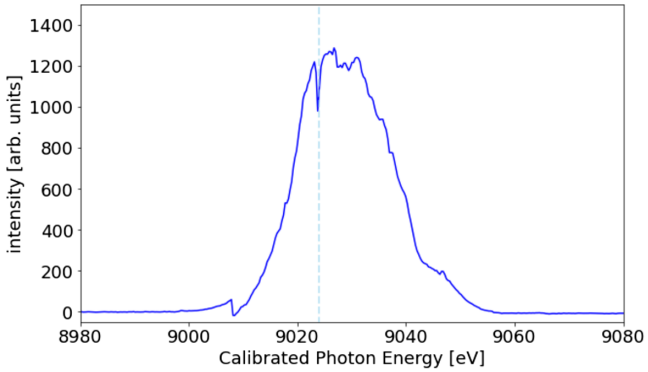

FIG. 6. Notch detected by a spectrometer for the C*(004) reflection at a pitch angle of 50°. The photon energy axis is calibrated postmeasurement using the model. The blue line is an average over multiple single-shots spectra.

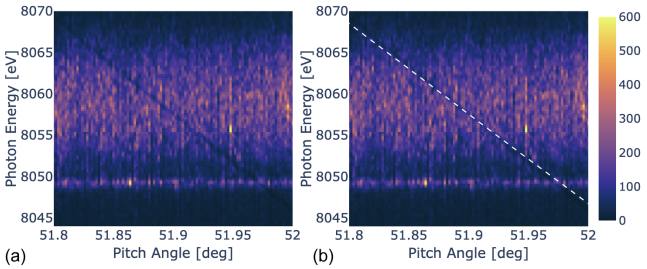

FIG. 7. Spectral notch measured at 8 keV: (a) the correlation between the measured photon energy and the pitch angle, (b) the calibrated photon energy (+1 eV), and the calculated C*(1-1-3) reflection plotted overlaying the scan.

E. Scintillator imager scan method

The third method considered here for absolute photon energy calibration only makes use of the scintillator imager discussed in Sec. II B and shown in Fig. 1. The advantage of this setup is that it does not require a spectrometer. Among the three methods, however, it is the one with the lowest resolution, which is limited by the SASE bandwidth. Keeping the undulator photon energy and the crystal roll angle fixed, the pitch angle is scanned through a reflection, making sure that the spot intensity increases and decreases again. An example is shown in Fig. 8 for the C*(1-1-3) reflection, showing three shots with different intensities as the crystal pitch angle is changed by 1.5°. Correlating the mean intensity of the images with the pitch angles, and translating the pitch angle using the model, one can determine the photon energy at the peak signal intensity.

The energy calibration approach using an imager was carried out on four different measurement campaigns, totalling 20 scans. The scans were performed at photon energies ranging from 7 to 18.2 keV, scanning 13 different crystal reflections. Figure 9 shows the positions of the spots as displayed by the camera output and categorized by the reflection identifier.

Figure 10 shows the calibrated measurements marked on top of the measurement model, as well as an example of the measured intensity for reflection C*(113) fitted to a Gaussian function. As discussed above, the energy resolution of this method is limited by the SASE bandwidth and since the SASE bandwidth is much larger than the HXRSS bandwidth, the scintillator imager method, while being the simplest to implement, is also the one with the lowest intrinsic resolution.

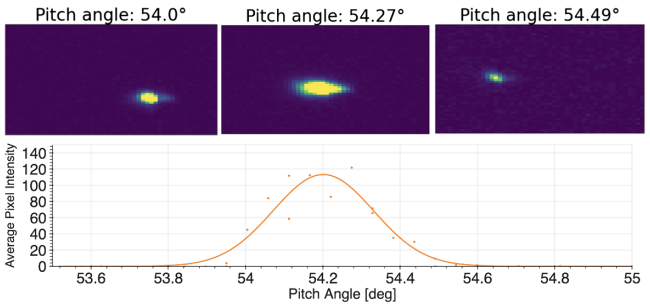

FIG. 8. Three shots from a pitch scan through reflection C*(1-1-3) as the crystal is rotated from 53.5° to 55°. A plot shows the variation of the intensity as the pitch angle was changed, as well as a Gaussian fit over the measured points.

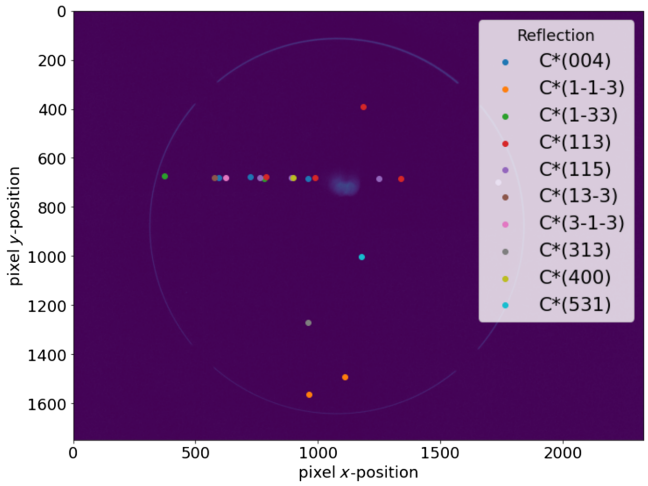

FIG. 9. Localization of reflections categorized by the reflection identifier.

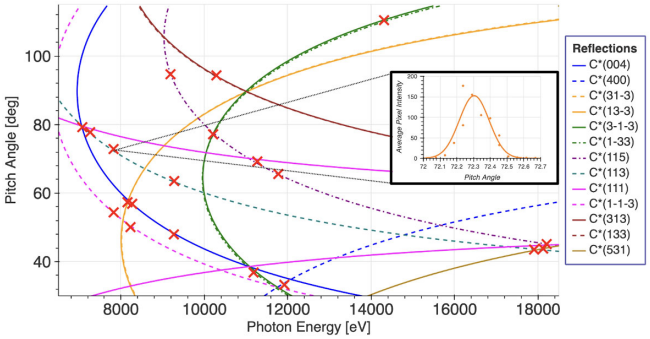

FIG. 10. Energy calibrations carried out with scintillator imager data and the surrogate model. The red cross indicates the calibrated photon energy at the peak measured pixel intensity. The inset shows the measured pixel intensities for the C*(113) reflection scan.

III. COPPER K-EDGE SCAN

Following the application of the three methods discussed in the previous section, we verified the spectrometer reflection classifier results by measuring x-ray absorption through a copper foil while scanning the photon energy around the K-edge. X-ray absorption edges of elements have been widely used for photon energy calibration of beamline crystal monochromators. This technique was used to experimentally verify the spectrometer reflection classifier method at the SASE2 undulator of the European XFEL during HXRSS operation at 9 keV. A simple schematic for the setup can be seen in Fig. 1. A 0.1 mm copper foil was inserted in front of a spectrometer and an energy scan around the K-edge (8979 eV) was performed. First, the absolute photon energy was determined using the method in Sec. II C 2 and used to calibrate the HIREX spectrometer. The undulator gaps in the first and second part of the undulator (before and after the self-seeding

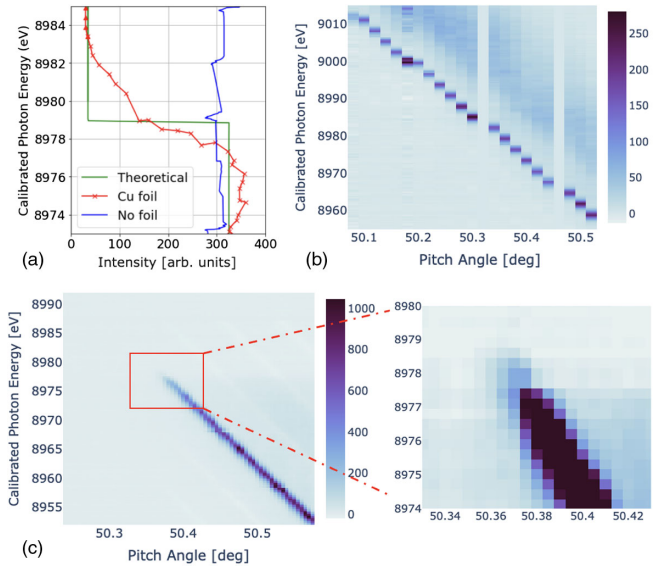

FIG. 11. (a) The measured spectral intensity plotted against the calibrated photon energy with the Cu foil inserted (red), no Cu foil (blue), and the theoretical absorption signal (green). (b) The correlation of the crystal pitch along the C*(004) reflection without the copper foil inserted in front of the spectrometer. (c) The correlation of the crystal pitch angle and calibrated seeding energy along the C*(004) reflection with the copper foil inserted in front of the spectrometer. The image shows the full range measured and a close-up version with a compressed color scale.

system) were changed and the pitch angle was also changed to match that. As a result, the C*(004) reflection was scanned for a range of 40 eV around the absorption edge. A copper foil was inserted in front of the HIREX detector, while another spectrometer used by the scientific instrument MID (materials imaging and dynamics) [28], GOTTHARD-II was measuring the spectrum with no copper foil. An x-ray gas monitor (XGM) was used to measure the total pulse energy of each separate FEL pulse in a train. The XGM exploits a dilute rare gas target, which undergoes ionization when exposed to the x-ray pulse. The resultant ions and electrons are directed toward two Faraday cups through an electrostatic field, and their currents are directly linked to the quantity of photons per pulse [29].

Starting with an initial photon energy of 8950 eV, the photon energy was increased in steps of 0.5 eV, pausing on each step for 30 s, to give time to the orbit feedbacks to react. While the seeding signal intensity measured by HIREX was noted to drop around the edge, the intensity in the second spectrometer, XGM, and camera was noted to be constant throughout the scan. Figure 11(a) shows the measured signal intensity with (red line) and without (blue line) the Cu foil inserted (the green line refers to the theoretical absorption curve [30]). The data points on the plot show the HIREX photon energy, obtained by fitting Gaussian curves to the spectra. The intensity is calculated

from the maximum peak of the fitted Gaussian curve. However, below the edge, the intensity was below the spectrometer noise and we show therefore the undulator set points corrected by the absolute energy calibration (triangle markers). Figure 11(b) shows the correlation of the crystal pitch angle and the calibrated HIREX seeding energy along the C*(004) reflection with no copper foil inserted. The scans without foil were performed with steps of 3 eV. Figure 11(c) shows the correlation of the crystal pitch angle and the calibrated HIREX seeding energy along the C*(004) reflection, including a close-up version where the seeding signal intensity was lost at the absorption edge energy of 8979 eV. The first inflection point is observed around 8977.5 eV while the tabulated value is 8979 eV. The difference of about 1.5 eV is within the accuracy of our calibration method (1–2 eV), limited by the bandwidth of the radiation pulse.

IV. CONCLUSION

Accurate knowledge of the photon energy of x-ray FEL pulses is often critically important for applications. This work has presented three different photon energy calibration methods that can make use of a Bragg crystal setup and a model-focused method. Based on Bragg's law, an analytical formulation is proposed to accurately represent the relation between the crystal pitch angle in the HXRSS system of the European XFEL and the seeded photon energy. This acts as a calibration standard. In the first method, called the spectrometer reflection classifier method, the measured angle or energy scan is processed to extract the reflection lines and a machine learning classifier decides the identity of the reflection based on the line properties. The *k*-nearest neighbor classifier is found to be the best classifier for this application. Some misclassifications occur in the presence of parallel reflections. However, this issue can be mitigated, in the future, by implementing a template matching method that compares measured scans and the model as a complete image without any feature extraction required [31]. This diagnostic was implemented in the control system of the European XFEL for the SASE2 undulator, and a verification of the calibration was carried out by scanning along the copper absorption K-edge. Similarly, the spectral notch created by the filtering process through the HXRSS crystal depends on the detection of a "shadow" following the same trajectory as the HXRSS signal in the photon energy-pitch angle plane while changing the crystal pitch angle. The final method uses a scintillator imager with a top view of the crystal to detect the different reflection intensities and correlate them to the model.

A virtual diagnostic to assist in crystal reflection identification and hence absolute energy spectra calibration can be used in a range of applications from machine optimizations to individual spectrometer calibrations. In fact, for the European XFEL, such a diagnostic is already envisioned to be part of a planned component ("x-ray Fiducialiser"), which is a Bragg crystal calibration device in the photon tunnel, to be used by two instruments.

ACKNOWLEDGMENTS

We thank Shan Liu and Wei Lun Qin for their support in HXRSS setup, as well as Sergey Tomin for his contributions towards pySpectrometer. We appreciate their fruitful discussions and support. This work was supported by the XFEL R&D funding proposal 321.

[1] M. Seto, J. Phys. Soc. Jpn. **82**, 021016 (2013).
[2] Y. Shvyd'ko *et al.*, Nature (London) **622**, 471 (2023).
[3] S. J. L. Billinge and I. Levin, Science **316**, 561 (2007).
[4] G. Geloni, V. Kocharyan and E. Saldin, Scientia **23**, 153 (1929).
[5] J. Arthur, Rev. Sci. Instrum. **60**, 2062 (1989).
[6] X. Huang, X. Shi, and L. Assoufid, J. Synchrotron Radiat. **29**, 159 (2022).
[7] W. L. Bond, Acta Crystallogr. **13**, 814 (1960).
[8] T. Masuda, T. Watanabe, K. Beeks, H. Fujimoto, T. Hiraki, H. Kaino, S. Kitao, Y. Miyamoto, K. Okai, N. Sasao, M. Seto, T. Schumm, Y. Shigekawa, K. Tamasaku, S. Uetake, A. Yamaguchi, Y. Yoda, A. Yoshimi, and K. Yoshimura, J. Synchrotron Radiat. **28**, 111 (2021).
[9] G. Geloni, V. Kocharyan, and E. Saldin, J. Mod. Opt. **58**, 1391 (2011).
[10] G. Geloni, Self-seeded free-electron lasers, in *Synchrotron Light Sources and Free-Electron Lasers: Accelerator Physics, Instrumentation and Science Applications*, edited by E. J. Jaeschke, S. Khan, J. R. Schneider, and J. B. Hastings (Springer International Publishing, Cham, 2016), pp. 161–193.
[11] W. Decking *et al.*, Nat. Photonics **14**, 391 (2020).
[12] S. Liu *et al.*, Nat. Photonics **17**, 984 (2023).
[13] J. Amann *et al.*, Nat. Photonics **6**, 693 (2012).
[14] I. Nam *et al.*, Nat. Photonics **15**, 435 (2021).
[15] A. A. Lutman, F.-J. Decker, A. Halavanau, T. J. Maxwell, and T. Sato, Opt. Express **30**, 43655 (2022).
[16] I. Petrov, L. Samoylova, S. Birnsteinova, V. Bellucci, M. Makita, T. Sato, A. Mazzolari, M. Romagnoni, R. Bean, A. Mancuso, A. Meents, H. N. Chapman, and P. Vagovic, arXiv:2303.00072.
[17] L. Samoylova, D. Shu, X. Dong, G. Geloni, S. Karabekyan, S. Terentev, V. Blank, S. Liu, T. Wohlenberg, W. Decking, and H. Sinn, AIP Conf. Proc. **2054**, 030016 (2019).
[18] A. Koch, W. Freund, J. Gruenert, M. Planas, T. Roth, L. Samoylova, and V. Lyamayev, in *Advances in X-ray Free-Electron Lasers Instrumentation III*, SPIE Proceedings Vol. 9512 (SPIE-International Society for Optical Engineering, Bellingham, WA, 2015).
[19] N. Kujala, W. Freund, J. Liu, A. Koch, T. Falk, M. Planas, F. Dietrich, J. Laksman, T. Maltezopoulos, J. Risch, F. Dall'Antonia, and J. Grünert, Rev. Sci. Instrum. **91**, 103101 (2020).

[20] S. Tomin and S. Serkez, PySpectrometer (pyHIREX), https://github.com/sergey-tomin/pyhirex (2022).
[21] A. L. Edelen, S. G. Biedron, S. V. Milton, and J. P. Edelen, First steps toward incorporating image based diagnostics into particle accelerator control systems using convolutional neural networks, arXiv:1612.05662.
[22] Y. Suzuki, H. Hino, T. Hawai, K. Saito, M. Kotsugi, and K. Ono, Sci. Rep. **10**, 21790 (2020).
[23] B. Sullivan, R. Archibald, J. Azadmanesh, V. G. Vandavasi, P. S. Langan, L. Coates, V. Lynch, and P. Langan, J. Appl. Crystallogr. **52**, 854 (2019).
[24] Z. Liu, H. Sharma, J.-S. Park, P. Kenesei, A. Miceli, J. Almer, R. Kettimuthu, and I. Foster, Int. Union Crystallogr. **9**, 104 (2022).
[25] J.-C. Yen, F.-J. Chang, and S. Chang, IEEE Trans. Image Process. **4**, 370 (1995).
[26] R. O. Duda and P. E. Hart, Commun. ACM **15**, 11 (1972).
[27] T. Bräunl, S. Feyrer, W. Rapf, and M. Reinhardt, Hough transform, in *Parallel Image Processing* (Springer, Berlin, Heidelberg, 2001), pp. 83–97.
[28] A. Madsen, J. Hallmann, G. Ansaldi, T. Roth, W. Lu, C. Kim, U. Boesenberg, A. Zozulya, J. Mcöller, R. Shayduk, M. Scholz, A. Bartmann, A. Schmidt, I. Lobato, K. Sukharnikov, M. Reiser, K. Kazarian, and I. Petrov, J. Synchrotron Radiat. **28**, 637 (2021).
[29] A. A. Sorokin, Y. Bican, S. Bonfigt, M. Brachmanski, M. Braune, U. F. Jastrow, A. Gottwald, H. Kaser, M. Richter, and K. Tiedtke, J. Synchrotron Radiat. **26**, 1092 (2019).
[30] B. Henke, E. Gullikson, and J. Davis, At. Data Nucl. Data Tables **54**, 181 (1993).
[31] C. Grech, G. A. Geloni, and M. W. Guetg, in *X-Ray Free-Electron Lasers: Advances in Source Development and Instrumentation VI*, edited by T. Tschentscher, L. Patthey, K. Tiedtke, and M. Zangrando, SPIE Proceedings Vol. 12581 (SPIE-International Society for Optics and Photonics, 2023), 125810G.